Electrochimica Acta 378 (2021) 138142

Contents lists available at ScienceDirect

Electrochimica Acta

journal homepage: www.elsevier.com/locate/electacta

Electrochemical preparation and homogenization of face-centered FeCoNiCu medium entropy alloy electrodes enabling oxygen evolution reactions

Jian Huang[a,b], Kaifa Du[a,b], Peilin Wang[a,b], Huayi Yin[a,b], Dihua Wang[a,b,*]

[a] School of Resource and Environmental Science, Wuhan University, Wuhan 430072, PR China
[b] International Cooperation Base for Sustainable Utilization of Resources and Energy in Hubei Province, Wuhan University, Wuhan 430072, PR China

ARTICLE INFO

Article history:
Received 17 November 2020
Revised 3 March 2021
Accepted 9 March 2021
Available online 12 March 2021

Keywords:
Medium entropy alloy
Molten salt electrochemistry
Oxide reduction
Oxygen evolution reaction
Alkaline solution

ABSTRACT

The exploitation of facile preparation methods and novel applications of entropy alloys has gained ever-increasing attention in recent years. In this paper, homogeneous FeCoNiCu medium entropy alloys (MEAs) with a face-centered cubic (FCC) structure are prepared by the electrochemical reduction of oxides in molten Na_2CO_3-K_2CO_3 using a low-cost Ni10Cu11Fe oxygen-evolution inert anode. The current efficiency reaches 85.3% with a low energy consumption of 2.9 kWh/kg-MEA. At the cathode, Ni acts as a solvent to dissolve other elements and facilitate the formation of the FCC phase, and the co-reduction process enhances the element diffusion rate thereby ensuring the homogeneity of the electrolytic MEAs. In addition, the electrolytic MEAs are pressed into pellet electrodes with an *in situ* formed oxides layer to catalyze oxygen evolution reactions (OER) in 1.0 M KOH solution. The electrocatalytic activity of the electrolytic MEAs outperforms the commercial IrO_2/Ta_2O_5-Ti electrode, i.e., the overpotential of the electrode is 439 mV at 50 mA/cm^2 and the electrode lasts for 10 h without any degradation. Therefore, this paper provides a facile approach to preparing homogeneous MEAs at below 1173 K using oxides feedstock, to accurately controlling compositions and structures of MEAs, and thereby to tailoring functionalities of MEAs.

1. Introduction

Medium entropy alloys (MEAs) that consist of three or four principal elements in equiatomic or near-equiatomic composition emerge as a promising functional material [1,2]. As an analogue of high-entropy alloys (HEAs), MEAs gradually attract significant attentions [3] due to their high yield strength [4,5], high thermal stability [6], excellent corrosion resistance [7–9], significant magnetic properties [10,11], etc. As we know, the functionalities of both MEAs and HEAs depend on the preparation methods, compositions, structures, and homogenization of the alloys. Thus, the exploitation of novel preparation methods and new functionalities of MEAs is of great importance to underpin the development of MEAs.

Common methods employ pure metals as feedstocks to prepare multi-component alloys such as MEAs and HEAs. The alloying of different metals is usually realized by several methods: (1) the arc melting method that involves a melting-solidification process [12], (2) the atomization method that melts and sprays the liquid metals [13,14], (3) the solid-state method either by sintering the solid metals at elevated temperatures or by milling the solid metal by mechanically forces [15,16], (4) the electrochemical deposition process [17], (5) the solvothermal synthesis process [18–20], (6) the carbon-thermal shock process [21] and (7) the fast moving bed pyrolysis process [22]. The melting-solidification process is easy to deploy and scale up, but it involves high-temperature and repeated remelting processes to ensure the homogenization of the alloys. The solid-state process is energy efficient and uses cheap equipment, but it is time-consuming and difficult to avoid the oxidation during the sintering or mechanical mixing process. The electrochemical deposition process is simple and energy efficient, but it is difficult to prepare a thick deposition layer and control the composition accurately. Thus, an energy-efficient method to prepare MEAs with controllable compositions and homogenous element distribution is urgently needed.

Electrochemical metallization of solid oxides in molten salts is a straightforward method for preparing metals or alloys using electrons as a green reducing agent [23]. One of the most notable

* Corresponding author at: School of Resource and Environmental Science, Wuhan University, Wuhan 430072, PR China.
E-mail address: wangdh@whu.edu.cn (D. Wang).

https://doi.org/10.1016/j.electacta.2021.138142
0013-4686/

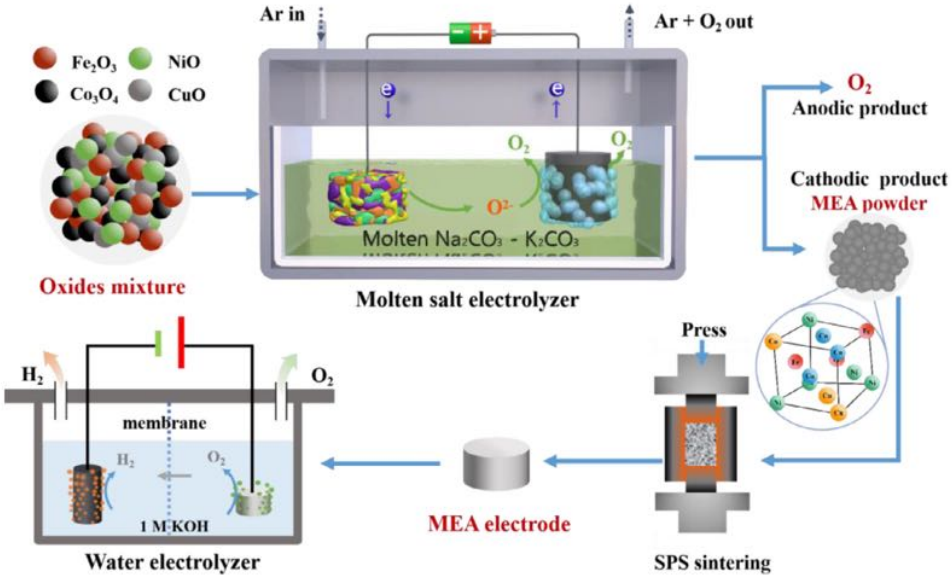

Fig. 1. Schematic illustration of the molten-salt electrolytic preparation of FeCoNiCu MEA electrodes enabling oxygen evolution in alkaline solutions.

advantages of the molten salt electrolysis of solid oxides for preparing alloys is the relatively low operating temperature, the ease of controlling compositions, and the homogenization of the alloys endowed by the mixed oxides and the electrochemical process. Thus, molten-salt electrolysis offers a straightforward way to prepare multi-component alloys such as MEAs and HEAs from the oxide mixtures through a solid-to-solid conversion, and the composition of products can be accurately controlled by controlling the ingredient of oxide precursors. In addition, several HEAs and MEAs (FeCoNiCrMn, TiNbTaZr, TiNbTaZrHf) have been synthesized in molten $CaCl_2$ at 1123 K [24,25], further confirming the potential of this method to prepare both MEA and HEA materials. However, developing a low-cost inert anode remains a challenge in molten chlorides [26,27]. A less corrosive molten Na_2CO_3-K_2CO_3 has been proven as a good electrolyte to allow the use of a low-cost Ni-base oxygen-evolution inert anode [28,29]. Albeit its low corrosivity, the molten Na_2CO_3-K_2CO_3 has a lower electrochemical window that can only be used to prepare metals whose oxide's Gibbs free energy formation is higher than that of Na_2O. In other words, only non-reactive metals can be prepared in molten Na_2CO_3-K_2CO_3 [30–34]. Thus, Fe- and Ni-based MEAs emerge as a promising functional material that can be prepared by electrolyzing oxides in molten Na_2CO_3-K_2CO_3 using a low-cost inert anode. In addition, the Fe- and Ni-derived oxides/hydroxides are a promising catalyst to enable oxygen evolution reactions (OERs) [35–38]. Therefore, it is of great interest to investigate the electrolytic Fe- and Ni-based MEAs for OERs in alkaline solutions.

In this paper, the FeCoNiCu MEA with a face-centered (FCC) cubic structure was first prepared by the electrochemical metallization of a mixture of oxides in molten Na_2CO_3-K_2CO_3 at 1123 K using an inert anode of Ni11Fe10Cu. Later, the obtained electrolytic powdery alloys were converted to pellet electrodes by a Spark Plasma Sintering (SPS) method. The effects of cell voltage, electrolysis time, temperature, and the composition of MEAs on the structure evolution and homogenization of alloys were studied. In addition, the obtained MEAs were tested as a catalytic electrode for OERs in alkaline aqueous solutions. The schematic illustration of the preparation process of MEA and its applications is shown in Fig. 1. This work provides a facile way to not only prepare MEAs with an energy-efficient and environment-friendly method, but also employ the electrochemical approach to tailoring the structure, composition, and properties of MEAs.

2. Experiment section

2.1. Preparation of powdery MEAs

Oxide pellets were prepared by a combined die-pressing and sintering approach. First, powders of Fe_2O_3, Co_3O_4, NiO and CuO (analytical purity, Sinopharm Chemical Regent Co. Ltd., China, and Fe:Co:Ni:Cu = 1:1:1:1 in molar ratio) were milled with agate balls and anhydrous alcohol for 10 h. After that, the mixed powder was die-pressed at 12 MPa into cylindrical pellets (1 g in weight and 10 mm in diameter). Second, the pellets were sintered at 1123 K in a muffle furnace for 2 h to enhance their mechanical strength. The compositions of oxide pellets were altered by controlling the molar ratio of the oxide feedstocks.

The electrochemical metallization of the oxide pellet was conducted in a stainless steel (SS) reactor flowed with Ar gas. First, an alumina crucible filled with 500 g of anhydrous Na_2CO_3-K_2CO_3 (Na:*K* = 58:42 in molar ratio) was placed in a graphite crucible which was then put at the bottom of the SS reactor heated by a vertical tube furnace. To remove moisture in the salt, the SS reactor was heated and maintained at 573 K for 48 h. Subsequently, the temperature was increased to and kept at the operating temperature of 1123 K in an argon atmosphere. Second, pre-electrolysis was conducted under a constant cell voltage of 2.0 V between a Ni10Cu11Fe alloy anode and a nickel foam cathode for 2 h to further remove the residual moisture and impurities of the molten Na_2CO_3-K_2CO_3. Third, the nickel foam cathode was replaced by an oxide pellet that was contained in a nickel box current collector (10 mm × 10 mm × 10 mm). The electrolysis was controlled and monitored by a computer-controlled DC power (Shenzhen Neware Electronic Ltd., China). When the electrolysis was terminated, the obtained products were washed with distilled water to remove the attached salts and dried in vacuum at 323 K for 10 h.

2.2. Cyclic voltammetry in molten Na_2CO_3-K_2CO_3

Cyclic voltammetry (CV) measurements were conducted on a CHI1140a electrochemical workstation (Shanghai Chenhua In-

strument Co., Ltd.) to investigate the reduction behaviors of Fe_2O_3, Co_3O_4, NiO, CuO and their mixtures. A Ni wire electrode (1 mm in diameter, 10 mm immersed into the melt) with or without an oxide coating was employed as working electrodes, a Ni10Cu11Fe alloy rod (20 mm in diameter) served as a counter electrode, and the reference electrode was a silver wire dipped into a mixture of Ag_2SO_4 (0.1 mol/kg) and eutectic melt (Li_2CO_3:Na_2CO_3:K_2CO_3=43.5:25:31.5, mol%) contained in a mullite cylinder. The oxide coating on the Ni wire electrode was prepared by repeatedly dipping the Ni wire into a solution containing oxide powders and ethanol. The ethanol solution was prepared by adding 3 g of oxides in 5 mL of ethanol under sonication for 10 min. After the dip-coating process, the Ni electrode was then dried under an infrared lamp to volatilize the ethanol.

2.3. Electrochemical performances of MEA in the alkaline solution

The obtained FeCoNiCu MEA powder was made into a cylinder pellet by Spark Plasma Sintering (SPS-3.20MK-2, Sumitomo Coal Mining Co. Ltd) at 60 MPa and 1123 K for 5 min under argon atmosphere. The pellet was then connected to a copper wire and embedded within paraffin to leave one face uncovered serving as an electrode. The apparent area of the electrode was 1.77 cm^2. Prior to each test, the electrode was mechanically polished to mirror-like smoothness with SiC papers up to #7000 and then washed with anhydrous alcohol. A standard three-electrode system consisted of an MEA working electrode, a Hg/HgO reference electrode, and a graphite rod counter electrode. Electrochemical measurements were conducted on a CHI660D electrochemical workstation (Shanghai Chenhua Instrument, China). All presented potentials in this paper referred to the reversible hydrogen potential (RHE). The OER electrocatalytic activities of FeCoNiCu MEA electrodes were examined by linear sweep voltammetry (LSV) with a scan rate of 5 mV/s in 1.0 M KOH solution. As a comparison, electrodes of Fe, Co, Ni, Cu wires and commercial IrO_2/Ta_2O_5-Ti were also tested in parallel. And the electrochemical impedance spectroscopy (EIS) measurements were performed by applying an AC voltage of 5 mV amplitude at 0.73 V within the frequency range of 0.01 to 1,00,000 Hz. Moreover, the stability of the FeCoNiCu MEA electrode was investigated by chronopotentiometry at 10 mA/cm^2 for 24 h and 50 mA/cm^2 for 10 h, respectively. All the electrochemical measurements were kept at 298 K in a thermostatic bath and the potential of measurements were compensated by 85% iR-drop.

2.4. Characterization

All obtained samples were characterized by X-ray diffraction spectroscopy (XRD, Shimadzu X-ray 6000 with Cu Kα1 radiation at λ=1.5405 Å), scanning electron microscopy (SEM, Evactron ES XEI), inductively coupled plasma-atomic emission spectrometer (ICP-AES, ICP-8000), energy dispersive X-ray spectroscopy (EDS, Aztec Energy X-Max 20), and oxygen/nitrogen analyzer (HORIBA EMGA-600 W/ST). Besides, the surface of the MEA electrode was analyzed by X-ray Photoelectron Spectroscopy (XPS) with a Krato Axis Ultra spectrometer (ESCALAB250Xi, Thermo Fisher Scientific, America) using a monochromatic Al Kα radiation.

3. Results and discussion

3.1. Thermodynamic analysis and electrochemistry of oxides in molten Na_2CO_3-K_2CO_3

Thermodynamic calculations are a powerful tool to screen suitable molten-salt electrolytes for the electrochemical reduction of oxides [30–33]. In principle, an oxide that can be reduced to its metallic form in molten Na_2CO_3-K_2CO_3 should have a more positive Gibbs free energy of formation than that of Na_2O. In other words, the target oxides to be reduced should be thermodynamically less stable than Na_2O. Thus, the metals that can be reduced in molten Na_2CO_3-K_2CO_3 can be predicted by the Ellingham diagram of oxides. Moreover, the Gibbs free energies of the formation of a compound are correlated to the theoretical decomposition voltages. As shown in Table S1, the theoretical decomposition voltages of Fe_2O_3, NiO, CuO and Co_3O_4 are smaller than those of Na_2CO_3 and K_2CO_3. Hence, Fe_2O_3, NiO, CuO, and Co_3O_4 can be thermodynamically reduced to their metallic forms in molten Na_2CO_3-K_2CO_3 without decomposing the molten salt electrolyte.

The electrochemical reduction behaviors of Fe_2O_3, NiO, CuO and Co_3O_4 in molten Na_2CO_3-K_2CO_3 were investigated by cyclic voltammetry. As shown in Fig. 2a–d, a pair of redox peaks (c3, a3) was correlated to the electrodeposition and stripping of Na when the potential was more negative than −1.9 V (*vs.* Ag/Ag_2SO_4). All potentials are referred to the Ag/Ag_2SO_4 couple if otherwise specified. In molten Na_2CO_3-K_2CO_3, Fe_2O_3, NiO, CuO and Co_3O_4 can be reduced prior to the deposition of Na, suggesting that these oxides can be reduced to metals without co-deposition of Na. And the sequence of the reduction potential of the oxides is consistent with the thermodynamic calculation (Table S1). In addition, the reduction of Fe_2O_3, CuO and Co_3O_4 involves two steps while NiO is reduced to Ni in one step. The peak c1 (−1.1 V) in Fig. 2a should be related to the formation of possible intermediate products such as $NaFe_2O_4$ or FeO [31,33], while the peak c2 (−1.5 V) is correlated to the formation of iron metal. The peak c1 (−1.3 V) in Fig. 2b is due to the formation of intermediate cobalt oxide compounds such as CoO or Na_xCoO_2, while the more negative peak c2 (−1.6 V) is assumed to the formation of cobalt metal [30]. The reduction peak c1 (−1.5 V) in Fig. 2c indicates the formation of nickel metal [33]. And the reduction peak c1 (−0.9 V) in Fig. 2d should be related to the formation of Cu_2O, and a more negative peak c2 (−1.4 V) attributes to the formation of Cu metal. As shown in Fig. 2e, f, the electrode coated with the oxide mixture has a weak reduction peak at −1.0 V and a major reduction peak at −1.5 V, indicating that the oxide mixture is co-reduced in a similar potential range. It is interesting that multiple redox peaks were not observed even there were four kinds of oxides. This means that there is a synergistic effect among the oxides that could affect the reduction behavior of oxide mixture. Note that the interaction of the oxides induces the reduction of different oxides at a similar potential, which could benefit the alloying and homogenization of electrolytic alloys.

3.2. Preparation of FeCoNiCu MEAs

3.2.1. Electrochemical reduction of oxide mixtures

FeCoNiCu MEAs of different compositions were prepared by a two-electrode electrolysis cell containing an oxide mixture cathode and a Ni10Cu11Fe inert anode. It was found that the oxide mixture contained $CuFe_2O_4$, $NiCo_2O_4$ and $NiFe_2O_4$ that were formed due to the sintering process of single oxides at 1123 K for 2 h (Fig. 3a). Except for CuO, the diffraction peaks of other oxides were not observed. So that the sintering process not only improved the mechanical strength of the pellet but also resulted in forming new chemical bonds that further mixed different elements at an atomic level. After electrolysis, the oxide mixture turned to the FCC-structured MEA alloy (Fig. 3a). As can be seen in Fig. 3b, the sintered oxides were mainly particles in size of 1–3 μm, while the particle size of reduced products increased to 2–10 μm with a nodular shape (Fig. 3c). Thus, the electrochemical metallization took place together with the growth and evolution of metal crystals [39]. The composition of the electrolytic products was close to the equal molar ratio as designed (Table S2). Furthermore, Fe, Co, Ni, and Cu in the alloy distributed uniformly in the alloy, further

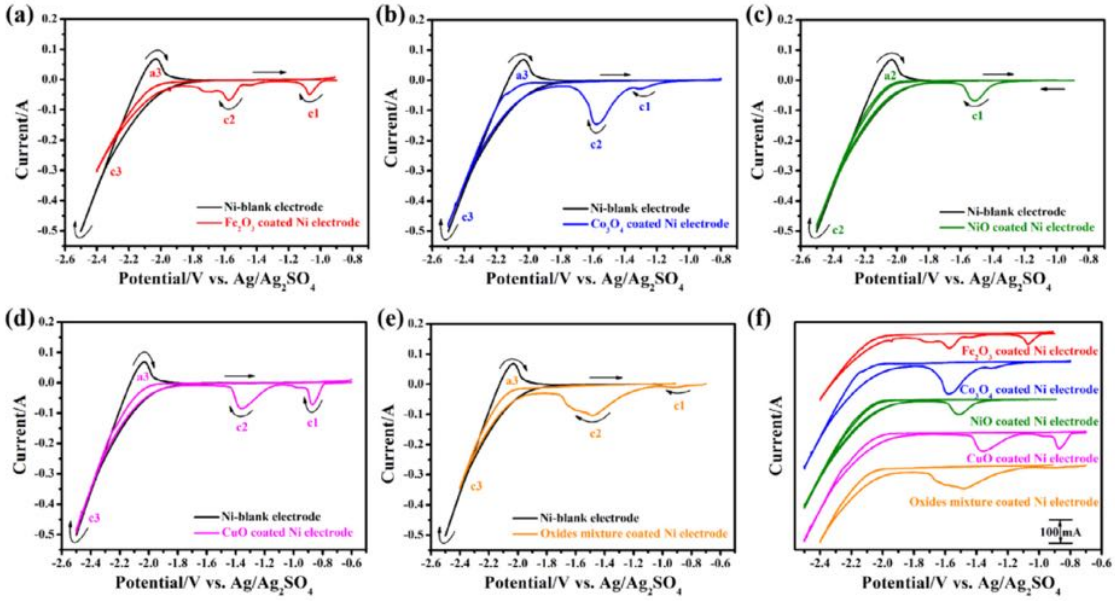

Fig. 2. Cyclic voltammograms of various oxides in molten Na_2CO_3-K_2CO_3 at 1123 K with a scan rate of 100 mV/s.

confirming that the pre-mixed oxide precursor and electrochemical reduction process are beneficial to ensure the homogenization of the electrolytic alloys (Fig. 3d–3h).

The electrolytic products obtained at different time were studied to reveal the reduction process of the oxide mixture. After 15 min, the electrolytic product contained $Co_{0.52}Cu_{0.48}$, $Cu_{0.81}Ni_{0.19}$, $Fe_{0.64}Ni_{0.3}$, and some unreduced oxides such as Co_3O_4, Cu_2O and $NiFe_2O_4$ (Fig. 4a). After 30 min, the FCC-phase alloy formed with some unreduced CoO and FeO (Fig. 4b). After 45 min, the product only contained FeO and the FCC phase alloy (Fig. 4c). After 60 min, the product was finally converted to a simple FCC phase alloy (Fig. 4d). This means that the formation of FCC-phase MEA involves multiple steps, and the reduction sequence obeys the thermodynamic calculation. First, binary alloys forms and then other metal oxides are reduced and the reduced metals simultaneously alloy with the binary alloy to form ternary and quaternary MEAs. Since the electrochemical reduction takes place step by step and all elements are well mixed in the oxide precursor, the electrochemical reduction process can prepare pure FCC-phase MEAs without obvious segregation.

In addition to the well-mixed precursors, the homogenization of the MEAs could also be correlated to the alloying and electrochemical processes. Thermodynamically, preferentially reduced Cu and Ni would act as solvents to dissolve Fe and Co to form binary alloys such as $Co_{0.52}Cu_{0.48}$, $Cu_{0.81}Ni_{0.19}$ and $Fe_{0.64}Ni_{0.36}$, as shown in Fig. 4a. Then, the binary alloys could act as a seed to promote the growth of the FCC-phase solid solution in which Ni acts as the solvent due to the effect of electro-assisted sintering [40,41]. As shown in Fig. S1, the particle size increases gradually with increasing the electrolysis time, confirming that metallization involves both reduction and alloying processes. For comparison, the metallic pellets consisting of the mixture of metal powders (original size was in a range of 10–100 nm) were sintered with or without applied potential in the molten salt at 1123 K for 6 h (Fig. 5). It is found that metal powder-derived alloys were not pure FCC-phase products, suggesting that the electrochemical reduction of oxides promotes the homogenization of the FCC-phase product. The metal-powder-derived products contained FCC_1+FCC_2 phase alloys because of the sluggish diffusion process among different metals. The formation of a single-phase solid solution could be due to the high entropy effect [42,43] and the electrochemical reduction process overcomes the energy barrier caused by the commonly solid-state reactions at 1123 K. Therefore, the oxide-derived homogeneous FCC alloys stems from the co-electrometallization and alloying processes.

3.2.2. Effects of the electrolytic parameters

The effects of temperatures, cell voltages and electrolysis time on the products and energy efficiency were investigated. As shown in Fig. 6a, the products obtained at 1023 K (black line) and 1073 K (red line) both had dual-phase structures (Cu-rich FCC_1 phase and Fe-rich FCC_2 phase), confirming that Cu and Fe are difficult to form a single-phase solid solution below 1073 K because of the large positive mixing enthalpy between Cu and Fe [44]. The proportion of the Cu-rich FCC_1 phase decreases (blue line) when increasing the temperature to 1123 K, suggesting that increasing the temperature facilitates the formation of sing-phase solid solution. Therefore, 1123 K was selected as the lowest electrolytic temperature for the preparation of oxide-derived FCC-phase MEAs. In addition to temperature, cell voltage also affects the formation of electrolytic products. As shown in Fig. 6b, the products obtained at 1.9 V for 4 h (black line) have a small amount of the Cu-rich FCC_1 phase, but prolonging the electrolytic time to 6 h at the same cell voltage (red line) can turn the FCC_1-rich phase to a simple FCC phase. This means that prolonging electrolytic time is beneficial to the formation of a single-phase solid solution. A higher cell voltage significantly accelerates the reaction rate and thereby promotes the formation of the single-phase alloy. Thus, the optimum cell voltage is 2.0 V. When the cell voltage is fixed at 2.0 V and the operating temperature is set at 1123 K, the effect of electrolysis time on the products is investigated. As shown in Fig. 6c, the diffraction peak of the product obtained at 2 h (red line) had a little left shoulder that could come from another phase other than the FCC phase. The diffraction peaks become more symmetrical and cleaner with increasing the electrolysis time, indicating that prolonging the electrolysis time can make a purer phase structure. Hence, the formation of single-phase MEAs is also related to the oxygen content and interdiffusion of metals because increasing electrolysis time also reduces the oxygen content of electrolytic products. As shown in Fig. 6d, the current declines close to the background current after 1 h, which suggests that the oxide is mostly metalized. In this

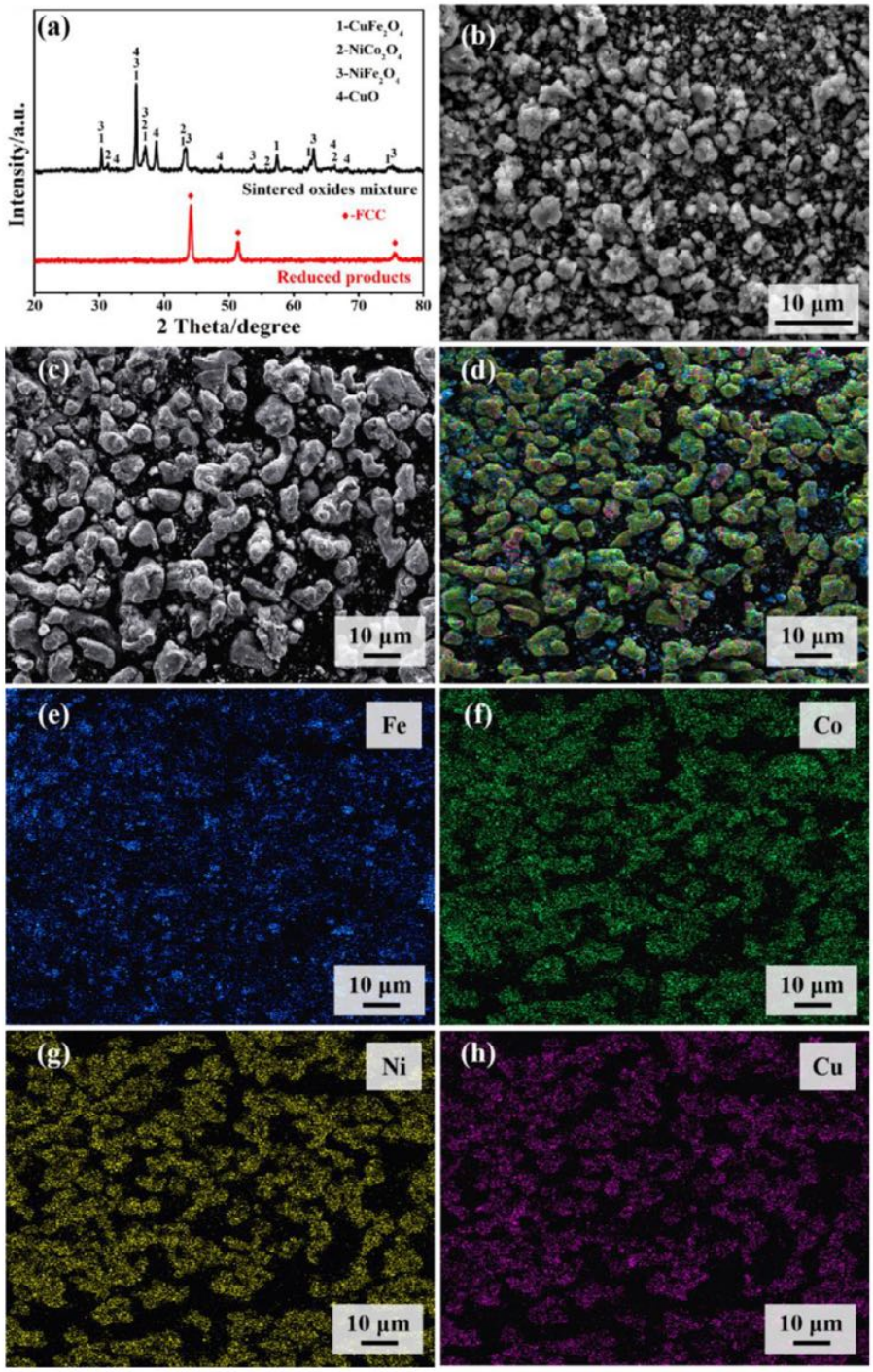

Fig. 3. (a) XRD patterns of the sintered oxide mixture (Fe_2O_3-Co_3O_4-NiO-CuO) before and after electrolysis at 1123 K and 2.0 V for 6 h in molten Na_2CO_3-K_2CO_3. (b) SEM image of the sintered oxides mixture. (c) SEM image of the reduced products. (d)–(h) EDS-Mapping of the electrolytic products.

condition, the current efficiency and energy consumption are calculated as 85.3% and 2.9 kWh/kg, respectively.

3.2.3. Regulating the composition of MEAs

The compositions and structures of electrolytic MEAs can be easily tailored by adjusting the composition of the oxide precursor. To simplify the expressions, products are denoted as MEA(Mx), where M represents the component element (*M*=Fe, Co, Ni and Cu), and x represents the molar ratio of M with the other component. As shown in Fig. 7a, all products have a single FCC structure when the content of Fe ranges from 0 to 1. However, the full width at half maximum (FWHM) gradually becomes widened with increasing Fe contents (Table S3), which suggests that increasing the Fe content decreases the grain size of MEAs [2]. As the mixing entropy of MEAs can reach its maximum when its component contents approach their equal proportion, the decrease of grain size is due to the enhancement of the sluggish diffusion effect [45]. Likewise, the MEAs with different Co contents are in the form of the single FCC structure (Fig. 7b). And the FWHM of its diffraction peaks become widened with increasing the Co content (Table S3). Thus, the grain size of MEAs could be effectively tailored by adjusting the content of Fe and Co. For Cu, the MEAs with a

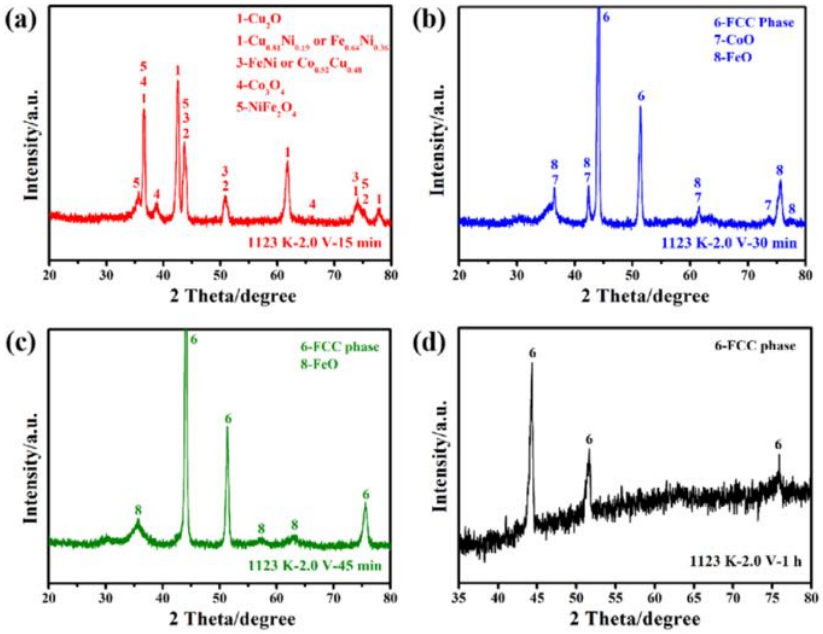

Fig. 4. XRD patterns of products at 1123 K and 2.0 V for different electrolysis time (a: 15 min, b: 30 min, c: 45 min and d: 60 min).

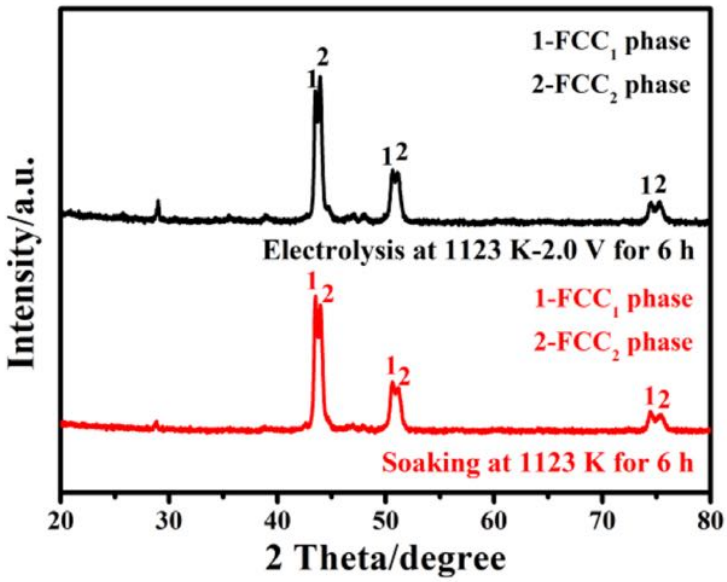

Fig. 5. XRD patterns of the pure metals mixture after sintering at 1123 K for 6 h and electrolysis at 1123 K and 2.0 V for 6 h in molten Na_2CO_3-K_2CO_3.

Cu content ranging from 0 to 1 are in the form of the single-FCC phase (Fig. 7c). Unlike the effect of Fe and Co, the diffraction peaks shift to lower angles with increasing the Cu content, indicating that the interplanar spacing of the products gradually increases. This is mainly due to the large atomic radius of Cu increases its interplanar spacing.

Different from Fe, Co and Cu, Ni has a significant effect on the phase structure of MEAs. As shown in Fig. 7d, the crystal structure of the products changes from dual-phases structure of FCC phase + Co-rich phase (MEA(Ni_0)) to Cu-rich FCC_1 phase + Fe-rich FCC_2 phase (MEA($Ni_{0.5}$)), Cu-rich FCC_1 phase + Fe-rich FCC_2 phase (MEA($Ni_{0.7}$)), and then a simple FCC phase (MEA(Ni_1)). The evolution of the phase structure suggests that increasing the Ni content facilitates the formation of FCC phase solid solution because Ni is a good solvent that can form infinite solid solutions with Fe, Co and Cu at 1123 K based on the phase diagrams of Ni-Fe, Ni-Co and Ni-Cu. In addition, the crystal structure of the solid solution is consistent with its solvent, while the contents of Fe, Co and Cu cannot affect the crystal structure of the products. Thus, Ni acts as the solvent in this MEA. Hence, the crystal structure and grain size of the MEAs can be effectively controlled by controlling the ingredient of oxide precursors, and thereby to further tailor the functionalities of MEAs.

3.3. Preparation of FeCoNiCu MEA electrodes

The electrolytic powdery MEAs were converted to MEAs pellet electrode by SPS, and the effects of the SPS process on the crystal structure of powdery MEAs to bulk MEAs were studied. As shown in Fig. 8. The powdery MEA has a single FCC phase (blue line). After the SPS treatment, the MEA maintains the FCC phase (black line), while the diffraction peaks shift to lower angles and also

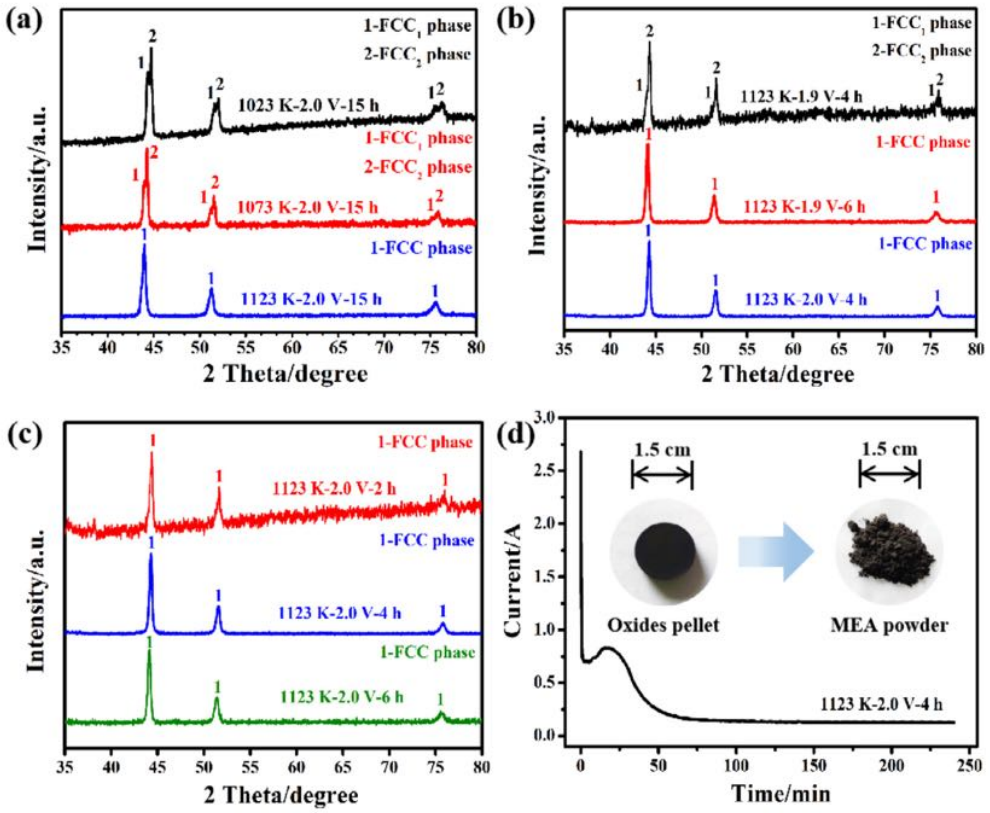

Fig. 6. XRD patterns of the reduced products at different (a) temperatures, (b) cell voltages and (c) electrolysis time. (d) Current-time curve of electrolysis at 2.0 V and 1123 K for 4 h.(For interpretation of the references to color in this figure, the reader is referred to the web version of this article).

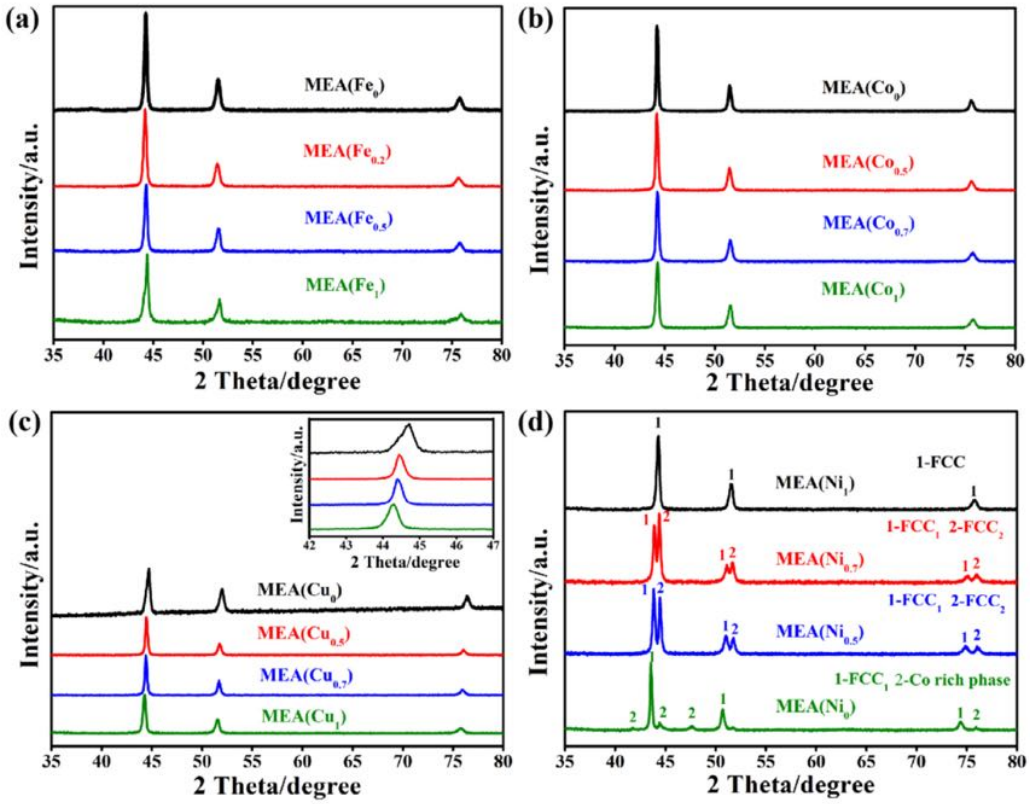

Fig. 7. XRD patterns of products with different component contents (a: Fe, b: Co, c: Cu and d: Ni) at 1123 K and 2.0 V for 4 h.

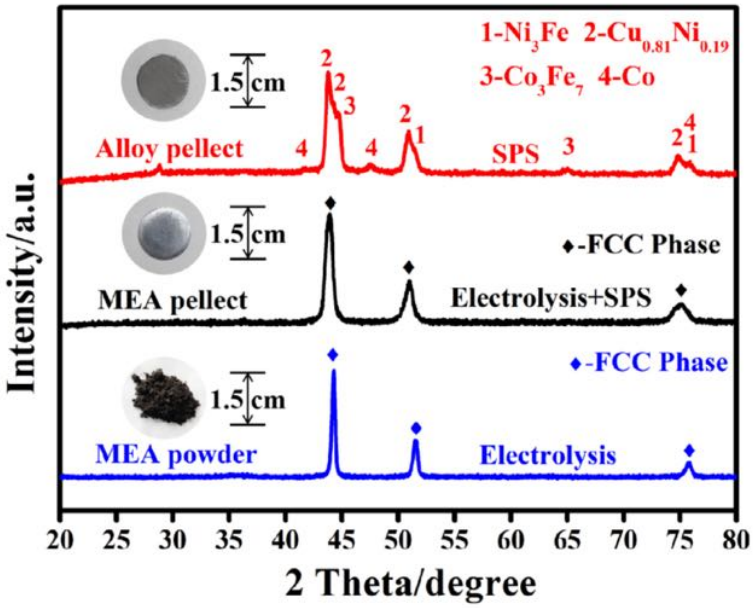

Fig. 8. Optical pictures and XRD patterns of the MEAs before and after SPS with different precursors.(For interpretation of the references to color in this figure, the reader is referred to the web version of this article).

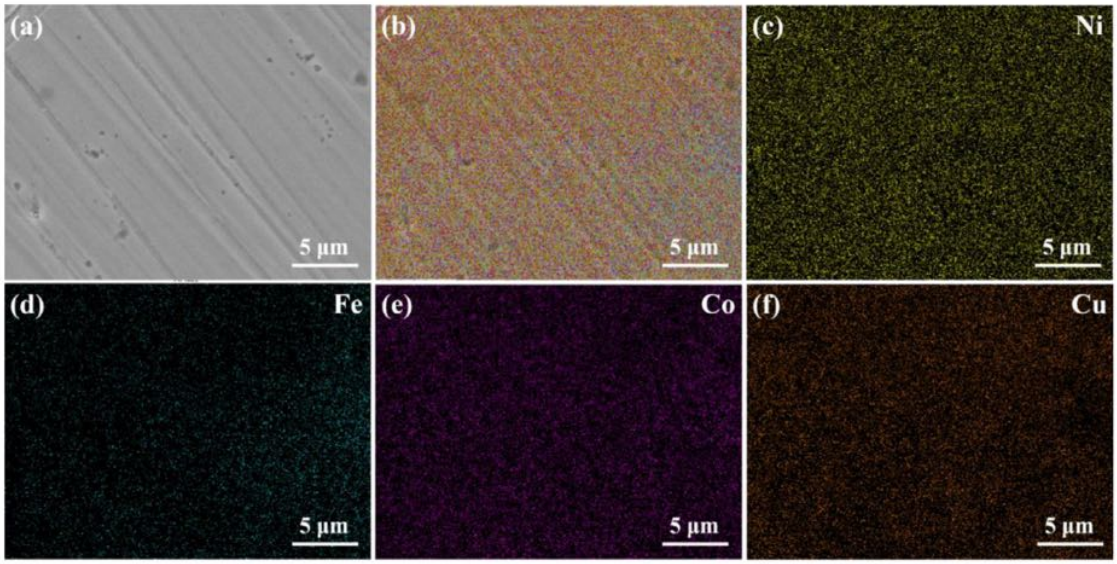

Fig. 9. EDS-Mapping of the MEA pellet after SPS at 1123 K and 60 MPa for 5 min.

are broadened, which indicates the increasing of interplanar spacing and the decreasing of grain size of MEAs. The high pressure of the SPS process results in the resultant lattice distortion of MEAs and increases interplanar spacing. Meanwhile, the fast heating and cooling rates of the sintering process enhance the sluggish diffusion effect, thus slowing the grain growth. In addition, the distribution of four elements in the bulk MEA pellet is uniform (Fig. 9), indicating the good thermal stability of the MEAs [46].

For comparison, the alloys were prepared with SPS using metal powder mixture as the feedstock. As shown in Fig. 8, only binary alloys such as Ni_3Fe, Co_3Fe_7 and $Cu_{0.81}Ni_{0.19}$ were obtained. Like the molten salt soaking process, using metal powders cannot prepare single FCC phase MEAs at 1123 K. As shown in Fig. 10, the distribution of four elements in the obtained bulk pellet is not uniform and has obvious segregation of Fe, Cu and Co. Therefore, the solid-state reaction at a temperature below 1123 K is difficult to prepare homogeneous MEAs from elemental powders.

3.4. OER electrocatalytic activity of FeCoNiCu MEAs

3.4.1. The effect of MEA composition on the OER activity

The as-prepared MEAs with various compositions were tested as catalytic electrodes for OER in 1.0 M KOH. As shown in Fig. S2, the bulk MEAs with different Fe (Fig. S2a), Co (Fig. S2b) and Cu (Fig. S2c) contents still remain the FCC phase after the SPS process, while their diffraction peaks shift to lower angles and become wider compared with that of the powdery MEAs (The FWHM of bulk MEAs are shown in Table S4). On the other hand, the MEAs with different Ni contents evolve from triple-phases structures (MEA(Ni_0)) to dual-FCC phases (MEA($Ni_{0.5}$) and MEA($Ni_{0.7}$)) and a simple FCC phase (MEA(Ni_1)) (Fig. S2d). As shown in Fig. 11a, the OER performance of MEAs increases with increasing Fe contents. As can be seen from Table S4, the grain size of MEAs decreases with increasing the Fe content. In this regard, the grain size of MEAs affects the OER performance. As 3d-transition-metal-

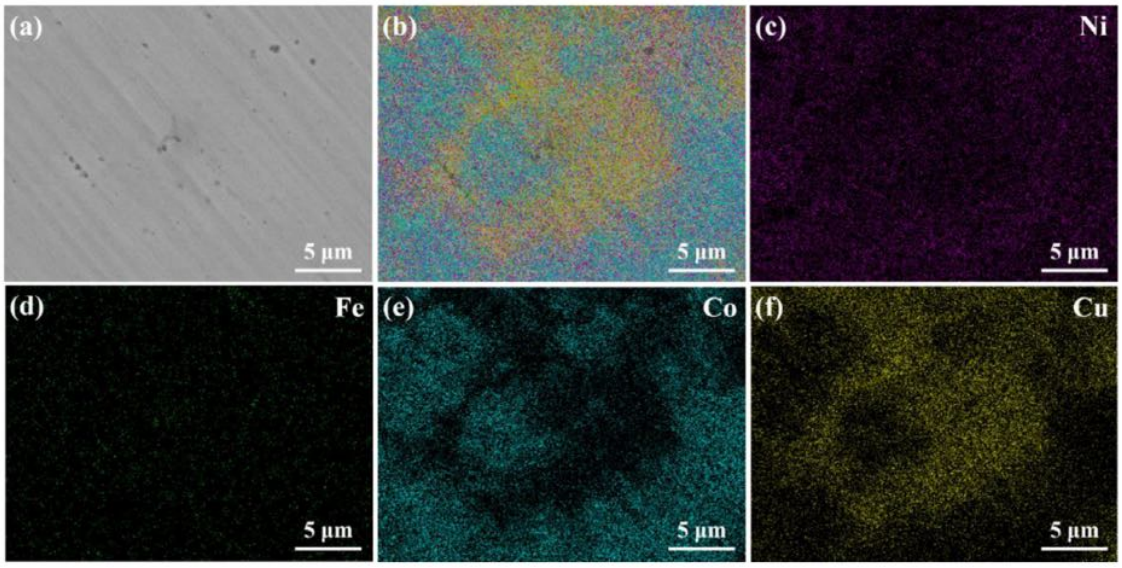

Fig. 10. EDS-Mapping of the metal-mixture-derived pellet prepared by SPS at 1123 K and 60 MPa for 5 min.

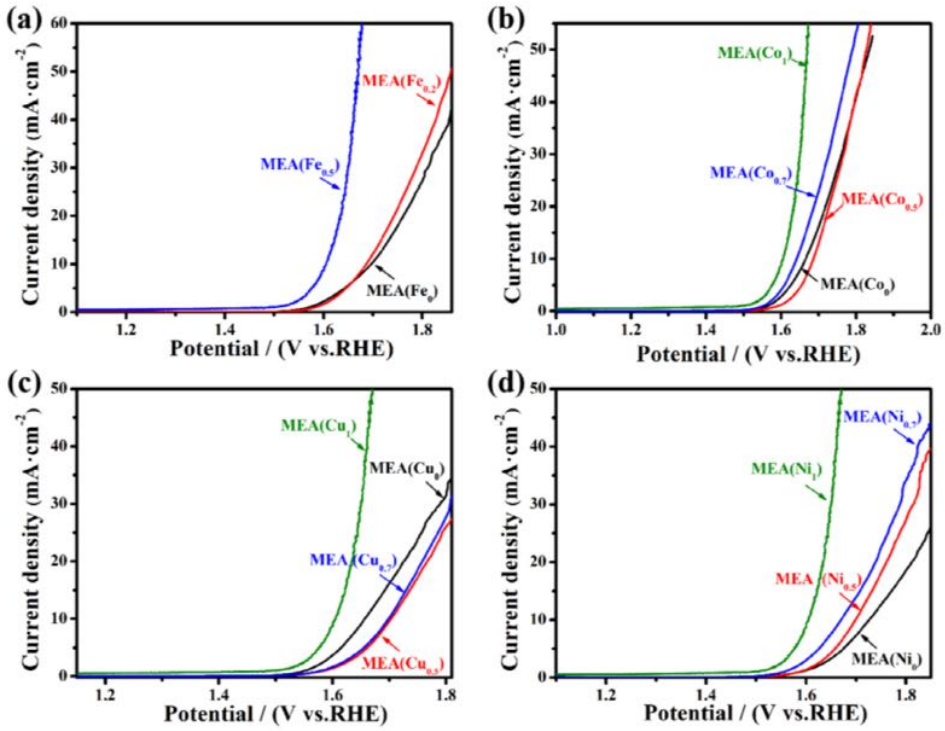

Fig. 11. LSV polarization curves of bulk MEAs electrodes with different component contents (a: Fe, b: Co, c: Cu and d: Ni) in 1.0 M KOH.

based catalysts have been widely reported [47,48], the theory of "cocktail effect" for HEAs could be correlated to their catalytic activity [49]. Note that the catalytic activity toward OER of the transition metals is due to the *in situ* formed oxide/hydroxide film, and the characterization of the catalytic film will be discussed later.

As shown in Fig. 11b, the OER performance increases with increasing the Co content. Thus, the similar effect of Ni to Fe and Co suggestes that the "cocktail effect" do affect the catalytic activity of MEAs. For Cu-containing MEAs, MEA(Cu_1) shows the best OER activity (Fig. 11c). However, the OER performance of MEAs electrodes containing Cu_x ($0< x < 1$) has the OER activity inferior to Cu_0 and Cu_1, meaning that the correlation of Cu content with the OER activity is not linear. In addition, the grain size of MEA(Cu_0) is smaller than MEA($Cu_{0.5}$) and MEA($Cu_{0.7}$), but is bigger than MEA(Cu_1), and this composition trend is consistent with the trend of OER performance among these MEAs (Table S4). Thus, further confirming the effect of the grain size of MEAs on its OER performance is needed. As shown in Fig. 11d, it is found that the OER performance of MEAs improves with increasing the contents of Ni, which may attribute to the "cocktail effect" as Ni has a high catalytic activity for OER. Additionally, only MEA(Ni_1) has a single FCC phase (Fig. 11d), and it shows the highest OER activity that is due to the homogeneous structure and the synergetic effect of the MEA. OER performances of MEAs electrodes with different compositions are summarized in Table S5. Therefore, the OER activity of MEA electrodes can be tailored by their compositions, grain size, and phase structures, and the MEAs electrode exhibits the best

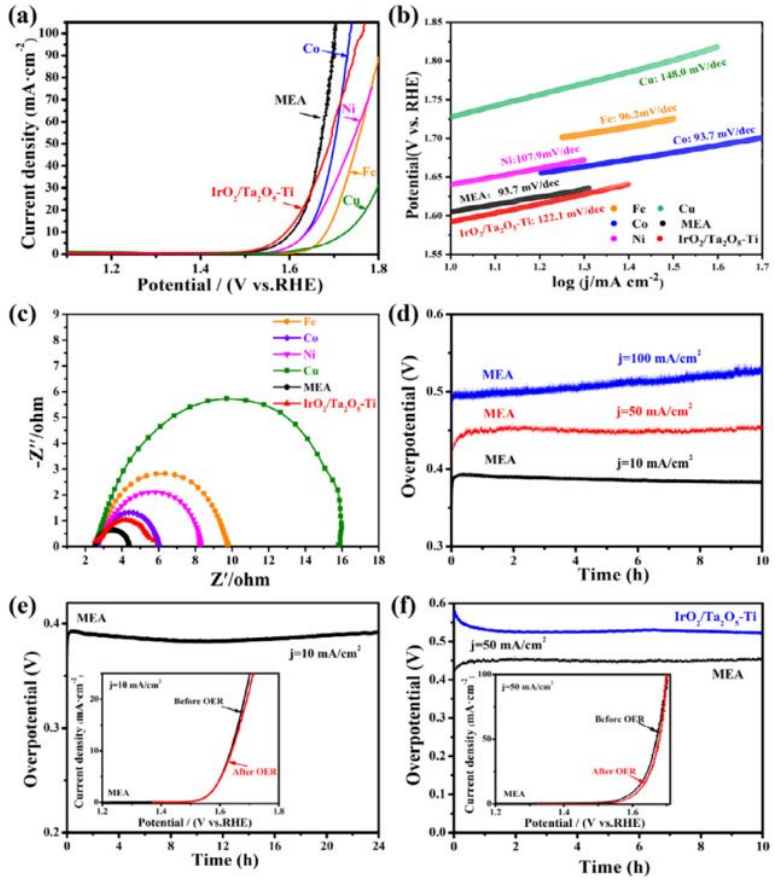

Fig. 12. (a) LSV polarization curves of bulk electrodes (MEA, Fe, Co, Ni, Cu and commercial IrO_2/Ta_2O_5-Ti) in 1.0 M KOH. (b) Tafel plots of LSV polarization curves of bulk electrodes applied for OER. (c) EIS spectra of bulk electrodes applied for OER. (d) Chronopotentiometry plots of MEA electrode operated at 10, 50 and 100 mA/cm^2 for 10 h. (e) Chronopotentiometry plots of MEA electrode operated at 10 mA/cm^2 for 24 h and the LSV polarization curves before and after chronopotentiometry. (f) Chronopotentiometry plots of MEA and commercial IrO_2/Ta_2O_5-Ti electrodes operated at 50 mA/cm^2 for 10 h and the LSV polarization curves of MEA electrode before and after chronopotentiometry. (For interpretation of the references to color in this figure, the reader is referred to the web version of this article).

OER activity when its component contents approach in equal proportion.

3.4.2. The stability of the MEA electrodes

As shown in Fig. 12a, the overpotential of MEA (black line) is 439 mV to drive a current density of 50 mA/cm^2, lower than that of the pure Fe (orange line), Co (blue line), Ni (purple line), Cu (green line) and the commercial IrO_2/Ta_2O_5-Ti (red line) electrodes. And the overpotential of MEA electrode is also smaller than FeCo [50], NiCo [50], $Cu_{47}Ag_{28}Zn_{25}$ [51], MnFeCoNi [52], FeCoNiCrAl [53] and FeNiMnCuCr [53] at 50 mA/cm^2. In addition, the lowest Tafel slope of MEA electrode (93.7 mV/dec) suggests the highest OER activity (Fig. 12b). Besides, EIS is used to estimate the interfacial properties of electrodes. The semicircle of the Nyquist plot is a benchmark of the charge transfer resistance (Rct) of the electrode. As shown in Fig. 12c, the Rct of the MEA electrode (1.86 Ω) is smaller than that of Fe (7.27 Ω), Co (3.38 Ω), Ni (5.63 Ω), Cu (13.3 Ω) and IrO_2/Ta_2O_5-Ti (3.07 Ω) electrodes, indicating that the MEA electrode possesses a high charge-transfer rate between the electrolyte and the active multi-oxides surface layer. These findings agree well with the linear-sweep results in Fig. 12a. Long-term electrolysis was carried out at different current densities at 10, 50 and 100 mA/cm^2 for 10 h, respectively (Fig. 12d). The MEA electrode exhibits a stable overpotential that keeps nearly constant at 10 and 50 mA/cm^2 for 10 h, while the potential gradually increases at 100 mA/cm^2. At a current density of 10 mA/cm^2, the MEA electrode has a stable overpotential for 24 h (Fig. 12e). The stability of the MEA electrode was also evaluated by measuring the LSV polarization curves before and after the chronopotentiometry measurement of 24 h (inset of Fig. 12e). At 50 mA/cm^2, the MEA electrode shows a better electrocatalytic activity with a lower overpotential than the IrO_2/Ta_2O_5-Ti for 10 h (Fig. 12f). In addition, there is almost no change among the LSV polarization curves before and after the chronopotentiometry measurement of 10 h (the inset profiles in Fig. 12f). Besides, the crystal structure and morphology of the MEA (Fig. S3) before and after the stability test of 10 h also show no significant change, further indicating the high stability of the MEA electrode.

3.4.3. Surface analysis of the MEA electrodes

The chemistry of the surface of MEA electrodes before and after OER tests was studied by XPS. Thermodynamically, the transition metals can be oxidized spontaneously by oxygen, so that the real catalytic layer is oxides and/or hydroxides. As shown in Fig. 13a, the peaks of binding energy for Fe $2p_{3/2}$ locate at 711.9 eV and 709.7 eV, which can be assigned to Fe_3O_4 and FeO, respectively [54]. The area ratio of Fe^{3+}/Fe^{2+} is nearly equal to 2.8. So the surface of the MEA electrode before OER contains FeO and Fe_3O_4. After OER, the ratio of Fe^{3+}/Fe^{2+} decreases to 2, indicating the formation of Fe_3O_4 (Fig. 13b). As shown in Fig. 13c, the two peaks located at 780.7 eV and 795.7 eV are assigned to Co $2p_{3/2}$ and Co $2p_{1/2}$ and correspond to CoO [55], while the peak at 778.2 eV can be assigned to metallic Co [56]. After the OER, the Co $2p_{3/2}$ peak can be divided into two peaks centered at 779.7 eV and 781.4 eV (Fig. 13d), corresponding to CoO and Co_2O_3, respectively [57]. The area ratio of Co^{3+}/Co^{2+} is nearly equal to 2, which corresponds to

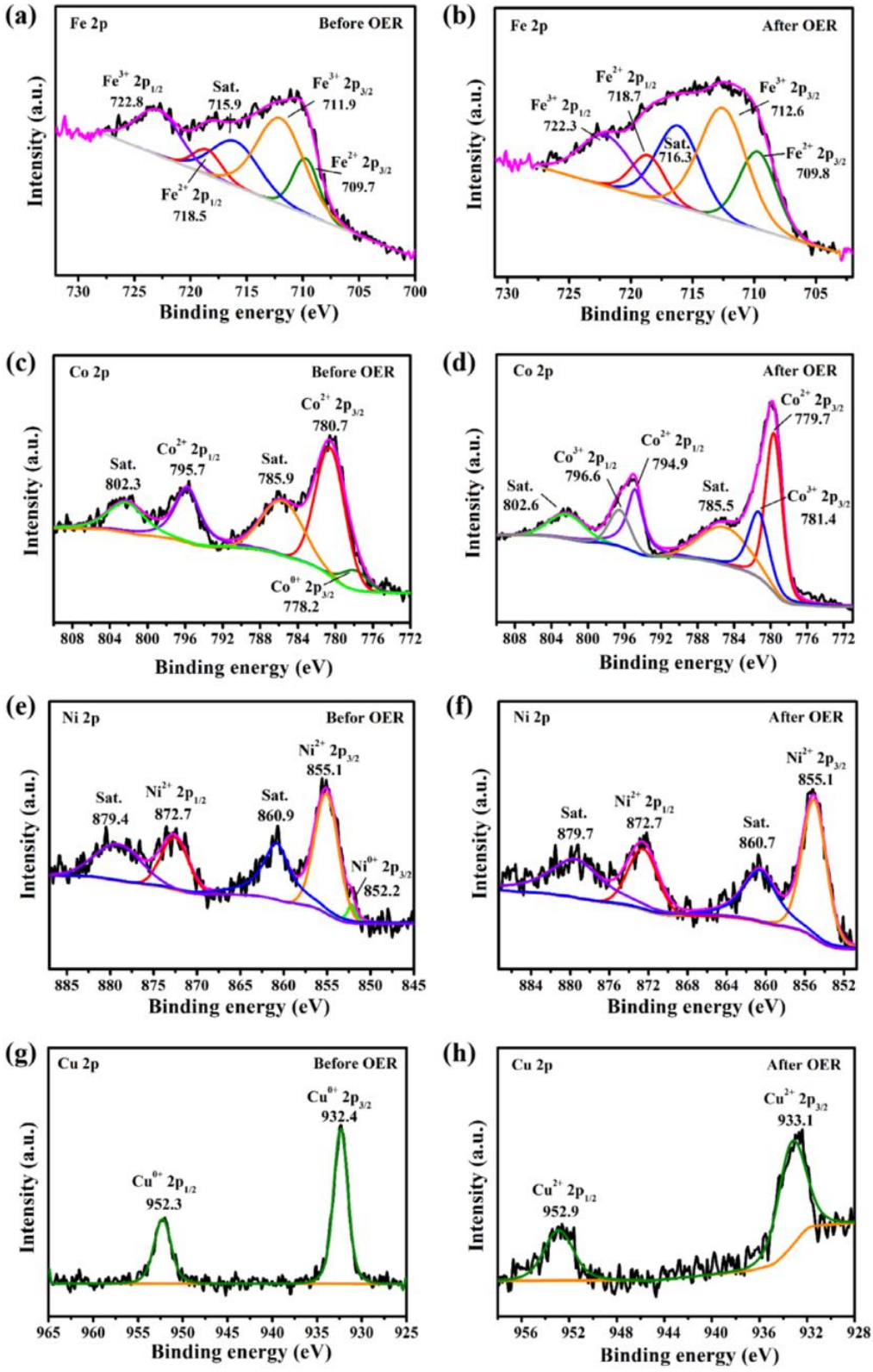

Fig. 13. XPS spectra of Fe 2p (a and b), Co 2p (c and d), Ni 2p (e and f) and Cu 2p (g and h) before and after OER performance of MEA electrodes, respectively.

Co_3O_4. Thus, the surface of MEA electrode contains CoO and Co before OER, and only Co_3O_4 exists after the OER. Two fitting peaks at about 855.1 eV and 872.7 eV are both observed in Fig. 13e and Fig. 13f, which correspond to the Ni $2p_{3/2}$ and Ni $2p_{1/2}$ of NiO, respectively. And the peak at 852.2 eV correlates to metallic Ni^0 (Fig. 13e) [58]. Thus, the surface of MEA electrode contains NiO and Ni before OER, and only NiO exists after the OER. In the Cu 2p spectra, Cu $2p_{3/2}$ and Cu $2p_{1/2}$ are observed at 932.4 eV and

952.3 eV, which correspond to metallic Cu^0 (Fig. 13g) [59]. While the peak of 933.1 eV (Cu $2p_{3/2}$) and 952.9 eV (Cu $2p_{1/2}$) in Fig. 13h can be assigned to CuO [60]. Hence, Cu^0 exists on the surface of the MEA electrode before OER, and Cu is converted to CuO after the OER. Therefore, the existence of CoO, NiO, FeO and Fe_3O_4 on the surface of the MEA electrode before the OER attributes to the oxidization of the MEA electrode in air. After OER, the oxide scale contains Fe_3O_4, Co_3O_4, NiO, and CuO and their combinations, which enables the oxygen evolution with catalytic performances as good as the commercial IrO_2/Ta_2O_5-Ti electrode. The good catalytic activity stems from the synergistic effect of both the alloys and the *in situ* formed oxide scale, and the underlying mechanism needs to be further understood in the future.

4. Conclusions

Molten-salt electrolysis has been proven as a green approach to preparing homogeneous powdery FeCoNiCu MEAs with a single FCC phase. The current efficiency reaches up to 85.3% with a low energy consumption of 2.9 kwh/kg-MEA. During the electrometallurgical process, Ni acts as a solvent to facilitate the formation of the FCC phase, and the co-reduction and alloying processes contribute to the homogenization of MEAs. Moreover, oxide-derived MEAs exhibit a low overpotential of 439 mV at 50 mA/cm^2, and the MEA electrode lasts for 10 h without any degradation in 1.0 M KOH. The good OER catalytic activity comes from the *in situ* formed oxide scale comprising of Fe_3O_4, Co_3O_4, CuO, and NiO, as well as the synergic effect of the multiple elements in the MEAs. In short, molten salt electrolysis is an energy-efficient approach to preparing homogeneous MEAs at below 1173 K, to accurately controlling the composition and structure of various entropy alloys, and then to further expanding its applications in addition to OER.

Declaration of Competing Interest

None

Acknowledgments

This work was supported by the National Natural Science Foundation of China [Grant no. 51874211, 52031008]

Credit author statement

Dihua Wang conceived the idea, Jian Huang, Kaifa Du, and Peilin Wang conducted experiments, Huayi Yin discussed the results and revised the protocol of the process, Jian Huang drafted the manuscript, and Dihua Wang revised and submitted the manuscript.

Supplementary materials

Supplementary material associated with this article can be found, in the online version, at doi:10.1016/j.electacta.2021.138142.

References

[1] J. Yeh, S. Chen, S. Lin, J. Gan, T. Chin, T. Shun, C. Tsau, S. Chang, Nanostructured high-entropy alloys with multiple principal elements: novel alloy design concepts and outcomes, Adv. Eng. Mater. 6 (5) (2004) 299–303, doi:10.1002/adem.200300567.

[2] Z. Fu, W. Chen, Z. Chen, H. Wen, E.J. Lavernia, Influence of Ti addition and sintering method on microstructure and mechanical behavior of a medium-entropy $Al_{0.6}$CoNiFe alloy, Mat. Sci. Eng. A 619 (2014) 137–145, doi:10.1016/j.msea.2014.09.077.

[3] N. Jia, Y. Li, X. Liu, Y. Zheng, B. Wang, J. Wang, Y. Xue, K. Jin, Thermal stability and mechanical properties of low-activation single-phase Ti-V-Ta medium entropy alloys, JOM 71 (10) (2019) 3490–3498, doi:10.1007/s11837-019-03713-3.

[4] H. Yao, J.W. Qiao, M. Gao, J. Hawk, S.G. Ma, H. Zhou, MoNbTaV medium-entropy alloy, Entropy 18 (5) (2016) 189–203, doi:10.3390/e18050189.

[5] D. Lee, M.P. Agustianingrum, N. Park, N. Tsuji, Synergistic effect by Al addition in improving mechanical performance of CoCrNi medium-entropy alloy, J. Alloy. Compd. 800 (2019) 372–378, doi:10.1016/j.jallcom.2019.06.005.

[6] H.W. Deng, Z.M. Xie, M.M. Wang, Y. Chen, R. Liu, J.F. Yang, T. Zhang, X.P. Wang, Q.F. Fang, C.S. Liu, Y. Xiong, A nanocrystalline AlCoCuNi medium-entropy alloy with high thermal stability via entropy and boundary engineering, Mat. Sci. Eng. A 774 (2020) 138925–139032, doi:10.1016/j.msea.2020.138925.

[7] H. Luo, S.S. Sohn, W. Lu, L. Li, X. Li, C.K. Soundararajan, W. Krieger, Z. Li, D. Raabe, A strong and ductile medium-entropy alloy resists hydrogen embrittlement and corrosion, Nat. Commun. 11 (1) (2020) 1–8, doi:10.1038/s41467-020-16791-8.

[8] H. Feng, H. Li, X. Wu, Z. Jiang, S. Zhao, T. Zhang, D. Xu, S. Zhang, H. Zhu, B. Zhang, M. Yang, Effect of nitrogen on corrosion behaviour of a novel high nitrogen medium-entropy alloy CrCoNiN manufactured by pressurized metallurgy, J. Mater. Sci. Technol. 34 (10) (2018) 1781–1790, doi:10.1016/j.jmst.2018.03.021.

[9] A. Fu, B. Liu, W. Lu, B. Liu, J. Li, Q. Fang, Z. Li, Y. Liu, A novel supersaturated medium entropy alloy with superior tensile properties and corrosion resistance, Scripta. Mater. 186 (2020) 381–386, doi:10.1016/j.scriptamat.2020.05.023.

[10] Q. Huang, D.P. Young, E.J. Podlaha, Magnetoresistance of electrodeposited iron–cobalt–nickel–copper multilayers, J. Appl. Phys. 94 (3) (2003) 1864–1867, doi:10.1063/1.1586956.

[11] Q. Huang, D.P. Young, J.Y. Chan, J. Jiang, E.J. Podlaha, Electrodeposition of FeCoNiCu/Cu compositionally modulated multilayers, J. Electrochem. Soc. 149 (6) (2002) C349–C354, doi:10.1149/1.1474433.

[12] Z. Jin, J. Lv, H. Jia, W. Liu, H. Li, Z. Chen, X. Lin, G. Xie, X. Liu, S. Sun, H.J. Qiu, Nanoporous Al-Ni-Co-Ir-Mo high-entropy alloy for record-high water splitting activity in acidic environments, Small 15 (2019) 1–7, doi:10.1002/smll.201904180.

[13] J.Y. He, W.H. Liu, H. Wang, Y. Wu, X.J. Liu, T.G. Nieh, Z.P. Lu, Effects of Al addition on structural evolution and tensile properties of the FeCoNiCrMn high-entropy alloy system, Acta. Mater. 62 (2014) 105–113, doi:10.1016/j.actamat.2013.09.037.

[14] L. Liu, Z.C. Zhang, J.C. Li, Q Jiang, Microstructure and the properties of FeCoCuNiSnx high entropy alloys, Mat. Sci. Eng. A. 548 (2012) 64–68, doi:10.1016/j.msea.2012.03.080.

[15] S. Varalakshmi, M. Kamaraj, B.S. Murty, Processing and properties of nanocrystalline CuNiCoZnAlTi high entropy alloys by mechanical alloying, Mat. Sci. Eng. A. 527 (4–5) (2010) 1027–1030, doi:10.1016/j.msea.2009.09.019.

[16] S. Varalakshmi, M. Kamaraj, B.S. Murty, Synthesis and characterization of nanocrystalline AlFeTiCrZnCu high entropy solid solution by mechanical alloying, J. Alloy. Compd. 460 (1–2) (2008) 253–257, doi:10.1016/j.jallcom.2007.05.104.

[17] Q. Huang, D. Davis, E.J. Podlaha, Electrodeposition of FeCoNiCu nanowires, J. Appl. Electrochem. 36 (8) (2006) 871–882, doi:10.1007/s10800-005-9098-3.

[18] D. Zhang, H. Zhao, B. Huang, B. Li, H. Li, Y. Han, Z. Wang, X. Wu, Y. Pan, Y. Sun, X. Sun, J. Lai, L. Wang, Advanced ultrathin RuPdM (M = Ni, Co, Fe) nanosheets electrocatalyst boosts hydrogen evolution, ACS Cent. Sci. 5 (2019) 1991–1997, doi:10.1021/acscentsci.9b01110.

[19] M. Bondesgaard, N.L.N. Broge, A. Mamakhel, M. Bremholm, B.B. Iversen, General solvothermal synthesis method for complete solubility range bimetallic and high-entropy alloy nanocatalysts, Adv. Funct. Mater. 29 (2019) 1–9, doi:10.1002/adfm.201905933.

[20] H. Li, Y. Han, H. Zhao, W. Qi, D. Zhang, Y. Yu, W. Cai, S. Li, J. Lai, B. Huang, L. Wang, Fast site-to-site electron transfer of high-entropy alloy nanocatalyst driving redox electrocatalysis, Nat. Commun. 11 (2020) 1–9, doi:10.1038/s41467-020-19277-9.

[21] Y. Yao, Z. Huang, P. Xie, S.D. Lacey, R.J. Jacob, H. Xie, F. Chen, A. Nie, T. Pu, M. Rehwoldt, D. Yu, M.R. Zachariah, C. Wang, R. Shahbazian-Yassar, J. Li, L. Hu, Carbothermal shock synthesis of high-entropy-alloy nanoparticles, Science 359 (80) (2018) 1489–1494, doi:10.1126/science.aan5412.

[22] S. Gao, S. Hao, Z. Huang, Y. Yuan, S. Han, L. Lei, X. Zhang, R. Shahbazian-Yassar, J. Lu, Synthesis of high-entropy alloy nanoparticles on supports by the fast moving bed pyrolysis, Nat. Commun. 11 (2020) 1–11, doi:10.1038/s41467-020-15934-1.

[23] B. Wang, J. Huang, J. Fan, Y. Dou, H. Zhu, D. Wang, Preparation of FeCoNiCrMn high entropy alloy by electrochemical reduction of solid oxides in molten salt and its corrosion behavior in aqueous solution, J. Electrochem. Soc. 164 (14) (2017) E575–E579, doi:10.1149/2.1521714jes.

[24] H. Jiao, M. Wang, J. Tu, S. Jiao, Production of AlCrNbTaTi high entropy alloy via electro-deoxidation of metal oxides, J. Electrochem. Soc. 165 (11) (2018) D574–D579, doi:10.1149/2.0021813jes.

[25] H. Yin, L. Gao, H. Zhu, X. Mao, F. Gan, D. Wang, On the development of metallic inert anode for molten $CaCl_2$–CaO System, Electrochim. Acta. 56 (9) (2011) 3296–3302, doi:10.1016/j.electacta.2011.01.026.

[26] S. Jiao, D.J. Fray, Development of an inert anode for electrowinning in calcium chloride–calcium oxide melts, Metall. Mater. Trans. B. 41 (1) (2009) 74–79, doi:10.1007/s11663-009-9281-8.

[27] D. Tang, K. Zheng, H. Yin, X. Mao, D.R. Sadoway, D. Wang, Electrochemical growth of a corrosion-resistant multi-layer scale to enable an oxygen-evolution inert anode in molten carbonate, Electrochim. Acta 279 (2018) 250–257, doi:10.1016/j.electacta.2018.05.095.

[28] K. Zheng, K. Du, X. Cheng, R. Jiang, B. Deng, H. Zhu, D. Wang, Nickel-Iron-Copper alloy as inert anode for ternary molten carbonate electrolysis at 650°C, J. Electrochem. Soc. 165 (11) (2018) E572–E577, doi:10.1149/2.1211811jes.
[29] X. Cheng, D. Tang, D. Tang, H. Zhu, D. Wang, Cobalt powder production by electro-reduction of Co_3O_4 granules in molten carbonates using an inert anode, J. Electrochem. Soc. 162 (6) (2015) E68–E72, doi:10.1149/2.0991506jes.
[30] D. Tang, H. Yin, W. Xiao, H. Zhu, X. Mao, D. Wang, Reduction mechanism and carbon content investigation for electrolytic production of iron from solid Fe_2O_3 in molten K_2CO_3–Na_2CO3 using an inert anode, J. Electroanal. Chem. 689 (2013) 109–116, doi:10.1016/j.jelechem.2012.11.027.
[31] H. Yin, D. Tang, H. Zhu, Y. Zhang, D. Wang, Production of iron and oxygen in molten K_2CO_3–Na_2CO_3 by electrochemically splitting Fe_2O_3 using a cost affordable inert anode, Electrochem. Commun. 13 (12) (2011) 1521–1524, doi:10.1016/j.elecom.2011.10.009.
[32] D. Tang, H. Yin, X. Cheng, W. Xiao, D. Wang, Green production of nickel powder by electro-reduction of NiO in molten Na_2CO_3–K_2CO_3, Int. J. Hydrogen. Energ. 41 (41) (2016) 18699–18705, doi:10.1016/j.ijhydene.2016.06.078.
[33] K. Zheng, X. Cheng, Y. Dou, H. Zhu, D. Wang, Electrolytic production of nickel-cobalt magnetic alloys from solid oxides in molten carbonates, J. Electrochem. Soc. 164 (13) (2017) E422–E427, doi:10.1149/2.1141713jes.
[34] H. Gu, G. Shi, H.-.C. Chen, S. Xie, Y. Li, H. Tong, C. Yang, C. Zhu, J.T. Mefford, H. Xia, W.C. Chueh, H.M. Chen, L. Zhang, Strong catalyst–support interactions in electrochemical oxygen evolution on Ni–Fe layered double hydroxide, ACS Energy. Lett. (2020) 3185–3194, doi:10.1021/acsenergylett.0c01584.
[35] E. Detsi, J.B. Cook, B.K. Lesel, C.L. Turner, Y.-.L. Liang, S. Robbennolt, S.H. Tolbert, Mesoporous $Ni_{60}Fe_{30}Mn_{10}$-alloy based metal/metal oxide composite thick films as highly active and robust oxygen evolution catalysts, Energ. Environ. Sci. 9 (2) (2016) 540–549, doi:10.1039/C5EE02509E.
[36] P. Zhang, L. Li, D. Nordlund, H. Chen, L. Fan, B. Zhang, X. Sheng, Q. Daniel, L. Sun, Dendritic core-shell nickel-iron-copper metal/metal oxide electrode for efficient electrocatalytic water oxidation, Nat. Commun. 9 (1) (2018) 381–390, doi:10.1038/s41467-017-02429-9.
[37] W. Dai, T. Lu, Y. Pan, Novel and promising electrocatalyst for oxygen evolution reaction based on MnFeCoNi high entropy alloy, J. Power. Sources. 430 (2019) 104–111, doi:10.1016/j.jpowsour.2019.05.030.
[38] G. Qiu, D. Wang, X. Jin, G.Z. Chen, A direct electrochemical route from oxide precursors to the terbium–nickel intermetallic compound $TbNi_5$, Electrochim. Acta 51 (26) (2006) 5785–5793, doi:10.1016/j.electacta.2006.03.019.
[39] X. Ma, H. Xie, J. Qu, Q. Song, Z. Ning, H. Zhao, H. Yin, An electro-assisted powder metallurgical route for the preparation of porous Ti and NiTi in molten $CaCl_2$, Metall. Mater. Trans. B 50 (2) (2019) 940–949, doi:10.1007/s11663-019-01522-2.
[40] X. Ma, H. Wang, H. Xie, J. Qu, X. Chen, F. Chen, Q. Song, H. Yin, Engineering the porosity and superelastic behaviors of NiTi alloys prepared by an electro-assisted powder metallurgical route in molten salts, J. Alloy. Compd. 794 (2019) 455–464, doi:10.1016/j.jallcom.2019.04.166.
[41] S. Yoshida, T. Bhattacharjee, Y. Bai, N. Tsuji, Friction stress and hall-petch relationship in CoCrNi equi-atomic medium entropy alloy processed by severe plastic deformation and subsequent annealing, Scripta. Mater. 134 (2017) 33–36, doi:10.1016/j.scriptamat.2017.02.042.
[42] J. Sure, D.S.M. Vishnu, C. Schwandt, Direct electrochemical synthesis of high-entropy alloys from metal oxides, Appl. Mater. Today 9 (2017) 111–121, doi:10.1016/j.apmt.2017.05.009.
[43] L. Liu, L.J. He, J.G. Qi, B. Wang, Z.F. Zhao, J. Shang, Y. Zhang, Effects of Sn element on microstructure and properties of $Sn_xAl_{2.5}$FeCoNiCu multi-component alloys, J. Alloy. Compd. 654 (2016) 327–332, doi:10.1016/j.jallcom.2015.09.093.
[44] J.W. Yeh, Alloy design strategies and future trends in high-entropy alloys, JOM 65 (12) (2013) 1759–1771, doi:10.1007/s11837-013-0761-6.
[45] C. Zhang, F. Zhang, H. Diao, M.C. Gao, Z. Tang, J.D. Poplawsky, P.K Liaw, Understanding phase stability of Al-Co-Cr-Fe-Ni high entropy alloys, Mater. Des. 109 (2016) 425–433, doi:10.1016/j.matdes.2016.07.073.
[46] M. Gong, Y. Li, H. Wang, Y. Liang, J.Z. Wu, J. Zhou, J. Wang, T. Regier, F. Wei, H. Dai, An advanced Ni–Fe layered double hydroxide electrocatalyst for water oxidation, J. Am. Chem. Soc. 135 (23) (2013) 8452–8455, doi:10.1021/ja4027715.
[47] C.C. McCrory, S. Jung, J.C. Peters, T.F. Jaramillo, Benchmarking heterogeneous electrocatalysts for the oxygen evolution reaction, J. Am. Chem. Soc. 135 (45) (2013) 16977–16987, doi:10.1021/ja4027715.
[48] M.H. Tsai, J.W. Yeh, High-entropy alloys: a critical review, Mater. Res. Lett. 2 (3) (2014) 107–123, doi:10.1080/21663831.2014.912690.
[49] F. Dong, H. Wang, Z. Wu, J. Qiu, Marked enhancement of photocatalytic activity and photochemical stability of N-doped TiO_2 nanocrystals by Fe^{3+}/Fe^{2+} surface modification, J. Colloid. Interface. Sci. 343 (1) (2010) 200–208, doi:10.1016/j.jcis.2009.11.012.
[50] S. Gupta, L. Qiao, S. Zhao, H. Xu, Y. Lin, S.V. Devaguptapu, X. Wang, M.T. Swihart, G. Wu, Highly active and stable graphene tubes decorated with FeCoNi alloy nanoparticles via a template-free graphitization for bifunctional oxygen reduction and evolution, Adv. Energy Mater. 6 (22) (2016) 1601198, doi:10.1002/aenm.201601198.
[51] X. Huang, M. Xie, Y. Chen, Q. Zong, Z. Liu, Y. Jin, Copper-silver oxide nanowires grown on an alloy electrode as an efficient electrocatalyst for water oxidation, RSC Adv. 5 (2015) 26150–26156, doi:10.1039/c5ra00820d.
[52] W. Dai, T. Lu, Y. Pan, Novel and promising electrocatalyst for oxygen evolution reaction based on MnFeCoNi high entropy alloy, J. Power. Sources. 430 (2019) 104–111, doi:10.1016/j.jpowsour.2019.05.030.
[53] X. Cui, B. Zhang, C. Zeng, S. Guo, Electrocatalytic activity of high-entropy alloys toward oxygen evolution reaction, MRS Commun. 8 (2018) 1230–1235, doi:10.1557/mrc.2018.111.
[54] T.H. Xie, X. Sun, J. Lin, Enhanced photocatalytic degradation of RhB driven by visible light-induced MMCT of Ti(IV)-O-Fe(II) formed in fe-doped $SrTiO_3$, J. Phys. Chem. C. 112 (2008) 9753–9759, doi:10.1021/jp711797a.
[55] W. Wu, P. Xia, Y. Xuan, R. Yang, M. Chen, D. Jiang, Hierarchical CoO@Ni$(OH)_2$ core–shell heterostructure arrays for advanced asymmetric supercapacitors, Nanotechnology 31 (40) (2020) 405705–405713, doi:10.1088/1361-6528/ab99f2.
[56] M.C. Biesinger, B.P. Payne, A.P. Grosvenor, L.W.M. Lau, A.R. Gerson, R.S.C. Smart, Resolving surface chemical states in XPS analysis of first row transition metals, oxides and hydroxides: cr, Mn, Fe, Co and Ni, Appl. Surf. Sci. 257 (7) (2011) 2717–2730, doi:10.1016/j.apsusc.2010.10.051.
[57] L. Pi, N. Yang, W. Han, W. Xiao, D. Wang, Y. Xiong, M. Zhou, H. Hou, X. Mao, Heterogeneous activation of peroxymonocarbonate by Co-Mn oxides for the efficient degradation of chlorophenols in the presence of a naturally occurring level of bicarbonate, Chem. Eng. J. 334 (2018) 1297–1308, doi:10.1016/j.cej.2017.11.006.
[58] X. Li, Y. Wang, J. Wang, Y. Da, J. Zhang, L. Li, C. Zhong, Y. Deng, X. Han, W. Hu, Sequential electrodeposition of bifunctional catalytically active structures in MoO_3/Ni–NiO composite electrocatalysts for selective hydrogen and oxygen evolution, Adv. Mater. 32 (39) (2020) 2003414–2003425, doi:10.1002/adma.202003414.
[59] S.M. Pawar, B.S. Pawar, B. Hou, J.Aqueel Kim, A.T. Ahmed, H.S. Chavan, Y. Jo, S. Cho, A.I. Inamdar, J.L. Gunjakar, H. Kim, S. Cha, H. Im, Self-assembled two-dimensional copper oxide nanosheet bundles as an efficient oxygen evolution reaction (OER) electrocatalyst for water splitting applications, J. Mater. Chem. A. 5 (25) (2017) 12747–12751, doi:10.1039/C7TA02835K.
[60] M.C. Biesinger, L.W.M. Lau, A.R. Gerson, R.S.C Smart, Resolving surface chemical states in XPS analysis of first row transition metals, oxides and hydroxides: Sc, Ti, V, Cu and Zn, Appl. Surf. Sci. 257 (3) (2010) 887–898, doi:10.1016/j.apsusc.2010.07.086.